

Dalton Transactions

Accepted Manuscript



This is an *Accepted Manuscript*, which has been through the Royal Society of Chemistry peer review process and has been accepted for publication.

Accepted Manuscripts are published online shortly after acceptance, before technical editing, formatting and proof reading. Using this free service, authors can make their results available to the community, in citable form, before we publish the edited article. We will replace this *Accepted Manuscript* with the edited and formatted *Advance Article* as soon as it is available.

You can find more information about *Accepted Manuscripts* in the [Information for Authors](#).

Please note that technical editing may introduce minor changes to the text and/or graphics, which may alter content. The journal's standard [Terms & Conditions](#) and the [Ethical guidelines](#) still apply. In no event shall the Royal Society of Chemistry be held responsible for any errors or omissions in this *Accepted Manuscript* or any consequences arising from the use of any information it contains.

Investigation of Composition Dependent Structural and Optical
Properties of the $Zn_{1-x}Cd_xS$, coaxial $Zn_{0.99-x}Cd_xCu_{0.01}S/ZnS$,
 $Zn_{0.99-x}Cd_xMn_{0.01}S$ Nanorods Generated by a One-Step
Hydrothermal Process

**Donglai Han^{ab}, Jian Cao^{*c}, Shuo Yang^{ab}, Jinghai Yang^{*c}, Bingji Wang^c, Lin Fan^c,
Qianyu Liu^c, Tingting Wang^c, Haifeng Niu^c**

^aChangchun Institute of Optics, Fine Mechanics and Physics, Chinese Academy of Sciences, Changchun 130033, P. R. China

^bUniversity of Chinese Academy of Sciences, Beijing 100049, P. R. China

^cInstitute of Condensed State Physics, Jilin Normal University, Siping 136000, P. R. China

Corresponding author E-mail: jhyang@jlnu.edu.cn, caojian_928@163.com Phone: +86 434 3290009. Fax: +86 434 3294566

Abstract:

High-quality $Zn_{1-x}Cd_xS$, coaxial $Zn_{0.99-x}Cd_xCu_{0.01}S/ZnS$ and $Zn_{0.99-x}Cd_xMn_{0.01}S$ nanorods (NRs) were synthesized through a one-step hydrothermal method. The composition of the alloyed NRs was adjusted by controlling the Zn/Cd molar ratios. The results showed that all of the samples had a good crystallinity with the typical hexagonal wurzite structure. The Zn/Cd molar ratios, Cu and Mn doping played an important role in affecting the final structure, morphology and optical property of the alloyed NRs. The successive shift of the XRD and PL patterns indicated that the NRs obtained were not a mixture of ZnS and CdS, but the $Zn_{1-x}Cd_xS$ solid solution. After doping Cu^{2+} (1%) ions into the $Zn_{1-x}Cd_xS$ NRs, the samples exhibited a highly crystalline coaxial $Zn_{0.99-x}Cd_xCu_{0.01}S/ZnS$ core-shell NRs and showed a strong green emission peak centered at 509.6 nm. After doping Mn^{2+} (1%) ions into the $Zn_{1-x}Cd_xS$ NRs, the samples exhibited a better crystal quality and showed a strong yellow-orange emission peak centered at 583 nm.

Introduction

One-dimensional (1D) semiconductor nanorods (NRs) have been extensively investigated because of their proven potential use as the nanoscale building blocks, interconnects and functional units in electronic, photonic, optoelectronic and electrochemical devices¹⁻³. Recently, the main effort in preparing 1D semiconductor NRs has focused on the well-defined heterostructures such as solid solution (*i.e.* alloy)⁴, coaxial core-shell⁵ and composite nanostructures⁶. 1D semiconductor heterostructures NRs often exhibit superior or new functional properties compared to their individual counterparts. Among the many 1D semiconductor nanomaterials, NRs of binary II-VI compounds, such as ZnO, ZnS, CdS have been widely studied⁷⁻⁹. The wurtzite type ZnS ($E_g=3.66$ eV) and CdS ($E_g=2.49$ eV) are important direct band-gap semiconductors, which have potential applications in ultraviolet-light-emitting diodes, electroluminescent devices, flat-panel displays¹⁰⁻¹⁴ *et al.* As a typical solid-solution semiconductor, the ternary $Zn_{1-x}Cd_xS$ compounds are important in exploration of the continuous tunable optical properties for the desired wavelength through the gradual variation of their compositions without changing the nanocrystal size. Particularly for the wavelength in the range of 500 and 530 nm, which are interest for the preparation of the green LEDs as “must-have” emitters for the next-generation displays and white solid-state lightings¹⁵.

In the past few years, the transition metal ions doped semiconductor NRs were investigated intensively since they can not only retain nearly all intrinsic advantages of semiconductor NRs but also possess additional advantages such as larger Stokes shift to avoid self-absorption/energy transfer, enhanced thermal and chemical stability and longer excited state lifetime¹⁶. Along this direction, Mn^{2+} and Cu^{2+} doped ZnS (CdS) nanocrystals (NCs) are demonstrated as the efficient phosphor because of the blue to

orange light emission¹⁷⁻¹⁸. For Mn²⁺ doped ZnS (CdS) NCs, the emission is restricted within the yellow-orange region (580-600 nm) coming from the Mn²⁺ ⁴T₁-⁶A₁ transition¹⁹⁻²¹. For Cu²⁺ doped ZnS (CdS) NCs, a wide range of the blue-green emission through the recombination of the electron in the conduction band or defects of the ZnS host and the hole in Cu *t*² state can be obtained²²⁻²³. In this paper, we firstly report the synthesis of the high-quality Zn_{1-x}Cd_xS, coaxial Zn_{0.99-x}Cd_xCu_{0.01}S/ZnS, Zn_{0.99-x}Cd_xMn_{0.01}S NRs with superior optical properties by hydrothermal method at 180 °C, and investigate their composition dependent structural and optical properties.

Experimental Section

Materials. Zinc nitrate, cadmium nitrate, cupric nitrate, manganese nitrate, thiourea and ethylenediamine (EN) are all analytical grade (Shanghai Chemical Reagents Co.), and used without further purification.

Preparation of Zn_{1-x}Cd_xS NRs. In a typical process, 1-x mmol of zinc nitrate and x mmol of cadmium nitrate were dissolved in 16 ml EN and water (1:1 in volume ratio). After stirring for 1 hour, 3 mmol of thiourea were put into the resulting complex. After stirring for 2 hour, the colloid solution was transferred into a 20-ml Teflon-lined autoclave and kept at 180 °C for 12 hour. After the reaction, the autoclave was taken out and cooled down to room temperature. The product was washed with ethanol and deionized water for several times and separated by centrifugation, and then dried at 80 °C for 1 hour.

Preparation of Zn_{0.99-x}Cd_xCu_{0.01}S and Zn_{0.99-x}Cd_xMn_{0.01}S NRs. In a typical process, 0.99-x mmol of zinc nitrate, x mmol of cadmium nitrate and 0.01 mmol of cupric (manganese) nitrate were dissolved in 16 ml EN and water (1:1 in volume ratio). Then, the experiment process was carried out following the above-mentioned methodology.

Characterization of products. X-ray diffraction (XRD) pattern was collected on a

MAC Science MXP-18 X-ray diffractometer using a Cu target radiation source. Transmission electron micrographs (TEM) and high-resolution transmission electron microscopy (HRTEM) images were taken on JEM-2100 electron microscope equipped with an X-ray energy dispersive spectrometer (EDS). The specimen was prepared by depositing a drop of the dilute solution of the sample in ethanol on a carbon-coated copper grid and drying at room temperature. X-ray photoelectron (XPS) analysis was performed on a Vgescalab MK II X-ray photoelectron spectrometer (XPS) using Mg $K\alpha$ radiation ($h\nu = 1253.6$ eV) with a resolution of 1.0 eV. The binding energy values obtained in the XPS analysis were corrected by referencing the C 1s peak to 284.60 eV. EDX microanalysis was performed by field emission scanning electron microscopy (FESEM, JSM-6700F). Photoluminescence (PL) measurement was carried out at room temperature, using 325 nm as the excitation wavelength, He-Cd Laser as the source of excitation.

Results and Discussion

Figure 1 show the XRD patterns of the $Zn_{1-x}Cd_xS$ (Fig. 1a), $Zn_{0.99-x}Cd_xCu_{0.01}S$ (Fig. 1b) and $Zn_{0.99-x}Cd_xMn_{0.01}S$ NCs (Fig. 1c). As seen from Fig. 1 red lines, all the diffraction peaks for the $Zn_{0.95}Cd_{0.05}S$ (Fig. 1a red line), $Zn_{0.94}Cd_{0.05}Cu_{0.01}S$ (Fig. 1b red line) and $Zn_{0.94}Cd_{0.05}Mn_{0.01}S$ NCs (Fig. 1c red line) can be well indexed as the hexagonal wurtzite phase structure, which are consistent with the standard card (JCPDS No. 36-1450). It is possible to predict the growth direction by performing comparison of the full width at half maximum (FWHM) for different XRD peaks²⁴. It is noticeable that the FWHM value of the (002) diffraction peak at about 28.6° for the $Zn_{0.95}Cd_{0.05}S$ (Fig. 1a red line), $Zn_{0.94}Cd_{0.05}Cu_{0.01}S$ (Fig. 1b red line) and $Zn_{0.94}Cd_{0.05}Mn_{0.01}S$ (Fig. 1c red line) NCs is smaller than the other peaks, suggesting a preferential growth direction along the c-axis, which is further demonstrated below by TEM and HRTEM studies. As

the value of x increased, the diffraction peaks are gradually shifted to the lower angles, indicating that the lattice constants of the $Zn_{1-x}Cd_xS$ (Fig. 1a), $Zn_{0.99-x}Cd_xCu_{0.01}S$ (Fig. 1b) and $Zn_{0.99-x}Cd_xMn_{0.01}S$ NCs (Fig. 1c) are increased with the Cd^{2+} doped-ratio increased. The ionic radius of the Cd^{2+} ions (0.97 Å) is larger than that of the Zn^{2+} ions (0.74 Å). The lattice expansion can be observed if the Cd^{2+} ions substituted for the Zn^{2+} sites in the ZnS NCs. The successive shifts of the XRD patterns also indicate that the crystals obtained are not a mixture of ZnS and CdS, but the $Zn_{1-x}Cd_xS$, $Zn_{0.99-x}Cd_xCu_{0.01}S$ and $Zn_{0.99-x}Cd_xMn_{0.01}S$ solid solution²⁵. As seen from Fig. 1 blue lines, all the diffraction peaks for the $Zn_{0.10}Cd_{0.90}S$ (Fig. 1a blue line), $Zn_{0.09}Cd_{0.90}Cu_{0.01}S$ (Fig. 1b blue line) and $Zn_{0.09}Cd_{0.90}Mn_{0.01}S$ (Fig. 1c blue line) NCs can be well indexed as the hexagonal wurtzite phase structure, which are consistent with the standard card (JCPDS No. 41-1049). Unlike the earlier reports²⁶⁻²⁷, we observe the transformation from the wurtzite ZnS (JCPDS No. 36-1450) to wurtzite CdS (JCPDS No. 41-1049) by changing the ratio of the Cd^{2+} ions easily, and the conversion of the ZnS to CdS takes place as the Cd^{2+} doped ratio increased to 30% (Fig. 1 green line). The values in electronegativity of Cd (1.69) and Zn (1.65) are very close, which is favorable to form a solid solution alloy²⁶. After doping the $Cd^{2+}/Cu^{2+}/Mn^{2+}$ ions into the ZnS NCs, there is no extra diffraction peak from the doped ions observed for all the samples in Fig. 1, suggesting that the $Cd^{2+}/Cu^{2+}/Mn^{2+}$ ions are incorporated into the ZnS lattice. It is worth to note that the intensity of the diffraction peaks from 24° to 32° for the $Zn_{0.70}Cd_{0.30}S$ (Fig. 1a green line), $Zn_{0.69}Cd_{0.30}Cu_{0.01}S$ (Fig. 1b green line) and $Zn_{0.69}Cd_{0.30}Mn_{0.01}S$ (Fig. 1c green line) NCs are different. As the Cd^{2+} doped ratio increased, the relative intensity ratio of the (002) diffraction peak with respect to the (100) and (101) diffraction peak for the $Zn_{0.10}Cd_{0.90}S$ (Fig. 1a blue line) and $Zn_{0.09}Cd_{0.90}Mn_{0.01}S$ NCs (Fig. 1c blue line) is larger than that of the $Zn_{0.09}Cd_{0.90}Cu_{0.01}S$

NCs (Fig. 1b blue line). So, the doping element (the Cu^{2+} and Mn^{2+} ions in this paper) would have an important effect on the growth of the different lattice plane.

The detailed microstructures of the prepared samples are characterized using transmission electron microscopy. Figs. 2a-b show the TEM images of the $\text{Zn}_{0.70}\text{Cd}_{0.30}\text{S}$ NRs. It can be seen that they are all straight and have a smooth surface without any nanoparticle impurities. Their diameter is in the range of 8-18 nm (average 13 nm). The HRTEM images and fast Fourier transform (FFT) electron diffraction pattern (Figs. 2c-d) show a highly crystalline NRs grown along the (002) direction. The stacking faults along the (002) direction can also be observed in Fig. 2d (yellow arrow), which may be caused by the substitution reaction. The measured (001) lattice distances of the $\text{Zn}_{0.70}\text{Cd}_{0.30}\text{S}$ alloy NRs are separated by a distance of about 6.5 Å, which are smaller than the (001) *d*-spacing values of the wurtzite CdS (6.7 Å), but larger than those of the wurtzite ZnS (6.2 Å). This suggests that the $\text{Zn}_{0.70}\text{Cd}_{0.30}\text{S}$ alloy NRs have been constructed homogeneously.

Figure 3 show the TEM, HRTEM, FFT and IFFT images of the $\text{Zn}_{0.10}\text{Cd}_{0.90}\text{S}$ NRs. The TEM images (Figs. 3a-b) reveal that their width is in the range of 17-30 nm, with an average value of 23 nm. The average width is about 2 times larger than that of the $\text{Zn}_{0.70}\text{Cd}_{0.30}\text{S}$ NRs (13 nm). It is worth to note that the NRs show rippled surfaces (shown by black arrows in Figs. 3a-b). The displayed clear lattice spacing of 3.4 Å (Fig. 3c) is close to that of the wurtzite CdS (002) plane²⁸. The FFT electron diffraction pattern (see inset image of Fig. 3c) generated from the inversion of the HRTEM image (Fig. 3c) demonstrate that the growth direction of the NRs is (002), a preferential growth direction. The HRTEM images (Figs. 3d-e) of the rippled area (shown by black arrows in Figs. 3a-b) exhibit several dislocations and lattice disorders including non-periodic twinning and stacking faults along the axial direction of the NRs²⁹. The

FFT electron diffraction pattern has been shown in the inset. Elongation of the FFT spots along the growth axis indicates the presence of defects. The defect structure can also be clearly seen in the IFFT image (Fig. 3f).

Figure 4a-b show the TEM and HRTEM images of the $\text{Zn}_{0.69}\text{Cd}_{0.30}\text{Cu}_{0.01}\text{S}$ NRs. The TEM image (Fig. 4a) shows that these NRs are smooth and uniform over their entire lengths and the diameter is in the range of 6-11 nm (average 9 nm), which is smaller than that of the $\text{Zn}_{0.70}\text{Cd}_{0.30}\text{S}$ NRs (average 13 nm) (Figs. 2a-b). The growth direction of the $\text{Zn}_{0.69}\text{Cd}_{0.30}\text{Cu}_{0.01}\text{S}$ NRs is perpendicular to the lattice fringes and the d spacing of the (002) plane is about 3.1 Å (Fig. 4b), which is close to the lattice spacing of the wurtzite ZnS (002) plane²⁷. Its corresponding FFT electron diffraction pattern (see inset image of Fig. 4b) generated from the inversion of the HRTEM image (Fig. 4b) further confirms that it has the growth direction of (002). Figs. 4c-f show the TEM, HRTEM and FFT images of the $\text{Zn}_{0.09}\text{Cd}_{0.90}\text{Cu}_{0.01}\text{S}$ NRs. The TEM images of the $\text{Zn}_{0.09}\text{Cd}_{0.90}\text{Cu}_{0.01}\text{S}$ NRs (Figs. 4c-d) show an apparent contrast between the inner core and the outer shell, which suggest the existence of a coaxial core-shell structure. The diameter of the core is in the range of 56-84 nm, the shell layer is in the range of 10-16 nm thick. The HRTEM images (Figs. 4e-f) also exhibit the core-shell feature of the coaxial nanocomposites. Its corresponding FFT electron diffraction pattern (see inset image of Fig. 4e) generated from the inversion of the HRTEM image (Fig. 4e) further confirms that the coaxial nanocomposites also have the growth direction of (002). The shell has an interlayer spacing of 3.1 Å, which agrees well with the lattice spacing of the (002) planes of the wurtzite ZnS ($d_{(002)} = 3.12$ Å for bulk wurtzite ZnS); the core displays an interlayer spacing of 3.4 Å, which is in agreement with the lattice spacing of the (002) planes of the wurtzite CdS ($d_{(002)} = 3.36$ Å for bulk wurtzite CdS). The closeness of the two lattice spacing enabled the growth of the coaxial ZnS shell on the

CdS core NRs via a minor atomic-level surface reconstruction³⁰. The detailed compositional analysis of the $\text{Zn}_{0.09}\text{Cd}_{0.90}\text{Cu}_{0.01}\text{S}$ NRs is further performed using EDS in a scanning TEM (STEM), which illustrates the actual distribution of Cd, Zn and S, respectively. Fig. 4g shows a bright-field TEM image of the single $\text{Zn}_{0.09}\text{Cd}_{0.90}\text{Cu}_{0.01}\text{S}$ nanorod, which reveals a clear core-shell structure. The Cd, Zn and S elemental mapping from this nanorod (Figs. 4h-j) demonstrate that the Cd elements are concentrated only at the core region while the Zn and S signals disperse at the entire nanorod, which again confirms the core-shell configuration with a thin ZnS sheath.

Figure 5 show the TEM, HRTEM and FFT images of the $\text{Zn}_{0.69}\text{Cd}_{0.30}\text{Mn}_{0.01}\text{S}$ NRs (Figs. 5a,c,d) and $\text{Zn}_{0.09}\text{Cd}_{0.90}\text{Mn}_{0.01}\text{S}$ NRs (Figs. 5b,e,f). The TEM images (Figs. 5a-b) show that the average diameter of the $\text{Zn}_{0.69}\text{Cd}_{0.30}\text{Mn}_{0.01}\text{S}$ and $\text{Zn}_{0.09}\text{Cd}_{0.90}\text{Mn}_{0.01}\text{S}$ NRs is 8 and 62 nm, respectively. The HRTEM images of the $\text{Zn}_{0.69}\text{Cd}_{0.30}\text{Mn}_{0.01}\text{S}$ NRs (Figs. 5c-d) and $\text{Zn}_{0.09}\text{Cd}_{0.90}\text{Mn}_{0.01}\text{S}$ NRs (Figs. 5e-f) show a highly crystalline NRs grown along the (002) direction. The FFT image (see inset image of Fig. 5c) further proves that the $\text{Zn}_{0.69}\text{Cd}_{0.30}\text{Mn}_{0.01}\text{S}$ NRs grow along the (002) axis, which is in agreement with the XRD analysis. For the $\text{Zn}_{0.69}\text{Cd}_{0.30}\text{Mn}_{0.01}\text{S}$ NRs, the (001) fringes are separated by a distance of about 6.4 Å, which is smaller than that of the CdS (6.7 Å), and larger than that of the ZnS (6.2 Å), demonstrating that the $\text{Zn}_{0.69}\text{Cd}_{0.30}\text{Mn}_{0.01}\text{S}$ NRs is the homogeneous solid solution. For the $\text{Zn}_{0.09}\text{Cd}_{0.90}\text{Mn}_{0.01}\text{S}$ NRs, the (100) fringes are separated by a distance of about 3.6 Å, which is close to that of the CdS crystal.

To investigate the surface information of the prepared samples, X-ray photoelectron (XPS) analysis was carried out. Fig. 6 show the XPS survey spectra of the $\text{Zn}_{0.70}\text{Cd}_{0.30}\text{S}$, $\text{Zn}_{0.69}\text{Cd}_{0.30}\text{Cu}_{0.01}\text{S}$ and $\text{Zn}_{0.69}\text{Cd}_{0.30}\text{Mn}_{0.01}\text{S}$ NRs (Fig. 6a), the high-resolution binding energy spectra for Zn, Cd and S species (Figs. 6b-d), respectively. The presence of the carbon and oxygen in the survey spectrum (Fig. 6a) is due to the carbon tape used for

the measurement and the adsorbed gaseous molecules such as O₂, CO₂ and H₂O, respectively³¹. As shown in Fig. 6b, the high-resolution XPS spectrum of the Zn 2p_{3/2} peak in Zn_{0.70}Cd_{0.30}S (Fig. 6b red line) and Zn_{0.69}Cd_{0.30}Cu_{0.01}S (Fig. 6b green line) NRs shows the peak at 1023.1 and 1022.0 eV, corresponding to the Zn 2p_{3/2} peak of ZnSO₄³² and ZnS³³, respectively. The asymmetrical high-resolution XPS spectrum of the Zn 2p_{3/2} peaks in Zn_{0.69}Cd_{0.30}Mn_{0.01}S NRs (Fig. 6b blue line) shows two peaks, of which the peak at 1020.8 and 1023.1 eV correspond to the Zn 2p_{3/2} peak of Zn³⁴ and ZnSO₄³², respectively. Since that the local environment around the Zn²⁺ ions would be different due to the substitution of the Cd²⁺, Cu²⁺ or Mn²⁺ ions in place of the Zn²⁺ ions in ZnS lattice. The high-resolution XPS spectra of the Cd 3d_{5/2} peak in Zn_{0.70}Cd_{0.30}S (Fig. 6c red line) and Zn_{0.69}Cd_{0.30}Cu_{0.01}S (Fig. 6c green line) NRs show two peaks. For the Zn_{0.70}Cd_{0.30}S NRs (Fig. 6c red line), the peaks centered at 404.6 and 406.2 eV correspond to the Cd 3d_{5/2} peak of CdO³⁵ and Cd(NO₃)₂³⁶, respectively, demonstrating that the Cd bond to the oxygen (i.e. Cd-O) at dangling bonds or defects. For the Zn_{0.69}Cd_{0.30}Cu_{0.01}S NRs (Fig. 6c green line), the peaks centered at 403.6 and 405.3 eV correspond to the Cd 3d_{5/2} peak of CdO₂³⁷ and CdS³⁸, respectively. For the Zn_{0.69}Cd_{0.30}Mn_{0.01}S NRs (Fig. 6c blue line), the peak centered at 404.9 eV corresponds to the Cd 3d_{5/2} peak of CdS²⁸, which is smaller than that for the Zn_{0.69}Cd_{0.30}Cu_{0.01}S NRs (405.3 eV). The electronegativity (χ) of the Mn ($\chi_p=1.55$) is smaller than that of the Cu ($\chi_p=1.9$). Doping of the less electronegative dopant Mn would reduce the binding energy of Cd³⁹. The high-resolution binding energy spectra of the S 2p peak for the Zn_{0.70}Cd_{0.30}S (red line) and Zn_{0.69}Cd_{0.30}Cu_{0.01}S (green line) NRs (Fig. 6d) can be decomposed into two Gaussian peaks. The peak centered at 162.2, 162.0 and 161.7 eV is coming from the S 2p peak of ZnS⁴⁰⁻⁴². The peak centered at 161.1, 160.8 and 160.6 eV is corresponding to the S 2p peak of CdS⁴³, which is smaller than that of the pure

CdS (161.8 eV)⁴⁴. Since the radius of the Zn²⁺ and Cu²⁺ ions is so close, the bond length of the Zn-S and Cu-S is more or less the same. Whereas, the radius of the Cd²⁺ (0.97 Å) and Mn²⁺ (0.80 Å) ions is 30% and 8% larger than that of the Zn²⁺ (0.74 Å) ions. Thus, the variation of the coordination environments around the S²⁻ ions would affect the position of the binding energy of S 2*p*, leading to the shift of the binding energy. The compositional analysis of the Zn_{0.69}Cd_{0.30}Cu_{0.01}S and Zn_{0.69}Cd_{0.30}Mn_{0.01}S NRs is performed by EDX, which can be seen in Figs. 6e-f. Only 0.8 at% Cu and 0.58 at% Mn is detected for the Zn_{0.69}Cd_{0.30}Cu_{0.01}S and Zn_{0.69}Cd_{0.30}Mn_{0.01}S NRs, respectively.

Figure 7 show the room temperature photoluminescence (PL) spectra of the Zn_{1-x}Cd_xS (x=0.01, 0.05, 0.10, 0.30, 0.50, 0.70, 0.90) NRs. The PL spectrum of the Zn_{0.99}Cd_{0.01}S NRs (Fig. 7 red line) shows a broad blue-green emission band, coming from the defect states emission: S vacancy, Zn vacancy and surface states⁴⁵⁻⁴⁶. The PL spectrum of the Zn_{0.10}Cd_{0.90}S NRs shows a strong green emission at 517 nm and a weak red emission at 650 nm. The green emission is attributed to the recombination of electrons and holes across the band edge⁴⁷. The red band is most likely due to the self-activated defect centers formed by the cadmium vacancy inside the lattice⁴⁸. As the Cd²⁺ doped ratio increased, the position of the emission peaks show a systematically red shift from Zn_{0.99}Cd_{0.01}S to Zn_{0.10}Cd_{0.90}S NRs, which provide clear evidence for the formation of the alloyed Zn_{1-x}Cd_xS NRs via intermixing the wider bandgap of ZnS (3.68 eV) with the narrower bandgap of CdS (2.44 eV), rather than forming separate ZnS, CdS or a core-shell structured nanocrystals⁴⁹.

The PL spectra of the Zn_{0.99-x}Cd_xCu_{0.01}S and Zn_{0.99-x}Cd_xMn_{0.01}S NRs are dramatically different from that of the Zn_{1-x}Cd_xS NRs, which can be seen in Fig. 8. For the Zn_{0.99-x}Cd_xCu_{0.01}S (x=0.05, 0.10) NRs (Fig. 8a red, green line), the PL spectra show a

broad emission band in the blue and green regions between 380 and 550 nm. The blue region peaks from 380 to 450 nm are attributed to the transition from the conduction band edge of ZnS to the surface states S and S vacancy⁵⁰. The green region peaks from 500 to 550 nm are corresponding to the recombination from the shallow donor level (sulfur vacancy or interstitial S) to the t^2 level of Cu^{2+} ⁵¹⁻⁵². For the $\text{Zn}_{0.09}\text{Cd}_{0.9}\text{Cu}_{0.01}\text{S}$ NRs (Fig. 8a dark yellow line), the strong green emission peak centered at 509.6 nm dominates the PL spectrum, which corresponds to the intrinsic near band edge (NBE) emission⁵³, and the weak red emission peak centered at 636 nm (see the inset figure in Fig. 8a) is coming from the extrinsic deep-level emission (DLE) (cadmium vacancy)⁴⁸. As the Cd^{2+} doped ratio increased from 30% to 90%, the intrinsic NBE emission peak intensity increases and the peak position has a 9 nm red-shift, while the extrinsic DLE peak almost has no change. This can be referred to the fact that the $\text{Zn}_{0.99-x}\text{Cd}_x\text{Cu}_{0.01}\text{S}/\text{ZnS}$ core-shell structure has formed when the Cd^{2+} doped ratio increased to 90%, which is in consistent with the TEM results (Figs. 4c-d). Since that the PL emission intensity would be affected by the surface effects, such as surface adsorption, existence of surface dangling bonds *etc.* The enhancement PL intensity of the $\text{Zn}_{0.99-x}\text{Cd}_x\text{Cu}_{0.01}\text{S}$ NRs is due to the fact that the higher band gap ZnS shell material would suppress the transferring of the charge carriers from the CdS to the surface states on the surface of CdS, so that exhibiting the significantly enhanced PL intensity of the green emission. In addition, the localized strain and interface effect would also influence the optical properties of the core-shell nanomaterials⁵⁴⁻⁵⁵. Here, we suggest that the residual stress caused by the small lattice mismatch between ZnS and CdS contribute to the red-shift of the green emission.

For the $\text{Zn}_{0.99-x}\text{Cd}_x\text{Mn}_{0.01}\text{S}$ NRs (Fig. 8b), only a strong yellow-orange emission peak centered at 583 nm can be observed, corresponding to the $\text{Mn}^{2+} {}^4\text{T}_1\text{-}{}^6\text{A}_1$ transition⁵⁶.

The TEM results (Fig. 5) show the highly crystalline NRs, so there is no defect related emission peak in Fig. 8b. Previously, Sooklal *et al*⁵⁷ studied the effect of the location of the Mn^{2+} ions on the photophysics of ZnS nanoparticles. They found that Mn^{2+} incorporation into the ZnS lattice lead to the orange emission while ZnS with surface-bound Mn^{2+} yielded the ultraviolet emission. According to Neto *et al*⁵⁸, the characteristic emission of the Mn^{2+} ions occurs only when the Mn dopant is incorporated in the CdS nanocrystals and it would be absent if the dopant is substitutionally incorporated near the surface of the nanocrystals. As a comparison with our own results, it can be suggested that the Mn^{2+} ions are incorporated into the NRs. By increasing the Cd^{2+} doped concentration, the PL intensity of the yellow-orange emission is obviously decreased and higher doping concentration results in a stronger quenching. The quenching of the intensity of the yellow orange emission may be attributed to the enhancement of the nonradiative recombination process caused by more defect centers emerged by the increased concentration of the Cd^{2+} ions.

Conclusions

In this paper, the $Zn_{1-x}Cd_xS$, coaxial $Zn_{0.99-x}Cd_xCu_{0.01}S/ZnS$ and $Zn_{0.99-x}Cd_xMn_{0.01}S$ NRs were fabricated successfully by a one-step hydrothermal method. The composition of the alloyed NRs was adjusted by controlling the Zn/Cd molar ratios. All of the samples had a good crystallinity with the typical wurzite structure. The Zn/Cd molar ratios and Cu/Mn doping played an important role in affecting the morphologies and optical properties of the alloyed NRs. The formation of the solid solution had been proved by the XRD and PL results. After doping Cu^{2+} (1%) ions into the $Zn_{0.1}Cd_{0.9}S$ NRs, the samples exhibited a highly crystalline coaxial $Zn_{0.99-x}Cd_xCu_{0.01}S/ZnS$ core-shell NRs and showed a strong green emission peak centered at 509.6 nm. After

doping Mn^{2+} (1%) ions into the $\text{Zn}_{1-x}\text{Cd}_x\text{S}$ NRs, the samples exhibited a better crystal quality and showed a strong yellow-orange emission peak centered at 583 nm.

Acknowledgment: This work was financially supported by the National Programs for High Technology Research and Development of China (863) (Item No. 2013AA032202), the National Natural Science Foundation of China (Grant No.61008051, 61178074, 11204104, 11254001).

Reference

- [1] H. Yan, H. S. Choe, S. W. Nam, Y. J. Hu, S. Das, J. F. Klemic, J. C. Ellenbogen, C. M. Lieber, *Nature*, 2011, **470**, 240.
- [2] C. L. Pang, H. Cui, G. Yang, C. Wang, *Nano Lett.*, 2013, **13**, 4708.
- [3] M. Feng, L. B. Luo, B. Nie, S. H. Yu. *Adv. Funct. Mater.*, 2013, **23**, 5116.
- [4] Y. C. Wang, J. Y. Xu, P. Y. Ren, Q. L. Zhang, X. J. Zhuang, X. L. Zhu, Q. Wan, H. Zhou, W. Hu, A. L. Pan, *Phys. Chem. Chem. Phys.*, 2013, **15**, 2912.
- [5] H. Y. Hu, Z. B. Jiao, T. Wang, J. H. Ye, G. X. Lu, Y. P. Bi, *J. Mater. Chem.*, 2013, **1**, 10612.
- [6] Z. Wang, S. W. Cao, S. C. J. Loo, C. Xue, *CrystEngComm*, 2013, **15**, 5688.
- [7] R. M. Yu, C. F. Pan, J. Chen, G. Zhu, Z. L. Wang, *Adv. Funct. Mater.*, 2013, **23**, 5868.
- [8] H. B. Shen, H. Y. Shang, J. Z. Niu, W. W. Xu, H. Z. Wang, L. S. Li, *Nanoscale*, 2012, **4**, 6509.
- [9] H. Choi, P. V. Kamat, *J. Phys. Chem. C*, 2013, **4**, 3983.
- [10] B. D. Liu, Y. Bando, X. Jiang, C. Li, X. S. Fang, H. B. Zeng, T. Terao, C. C. Tang, M. Mitome, D. Golberg, *Nanotechnology*, 2010, **21**, 375601.
- [11] M. Z. Wang, W. J. Xie, H. Hu, Y. Q. Yu, C. Y. Wu, L. Wang, L. B. Luo, *Appl. Phys. Lett.*, 2013, **103**, 213111.
- [12] H. H. Guan, P. D. Han, Y. P. Li, X. Zhang, Q. N. Zhang, L. P. Wang, R. Z. Zhang, *Optik*, 2013, **124**, 198.
- [13] B. N. Pal, Y. Ghosh, S. Brovelli, R. Laocharoensuk, V. Klimov, J. A. Hollingsworth, H. Htoon, *Nano Lett.*, 2012, **12**, 331.
- [14] A. Lshizumi, Y. Kanemitsu, *Adv. Mater.*, 2006, **18**, 1083.
- [15] H. Shen, S. Wang, H. Wang, J. Niu, L. Qian, Y. Yang, A. Titov, J. Hyvonen, Y.

- Zheng, and L. S. Li, *ACS Appl. Mater. Interfaces*, 2013, **5**, 4260.
- [16] W. Zhang, X. Zhou and X. Zhong, *Inorg. Chem.*, 2012, **51**, 3579.
- [17] A. Aboulaich, L. Balan, J. Ghanbaja, G. Medjahdi, C. Merlin and R. Schneider, *Chem. Mater.*, 2011, **23**, 3706.
- [18] C. Corrado, Y. Jiang, F. Oba, M. Kozina, F. Bridges, and J. Z. Zhang, *J. Phys. Chem. A.*, 2009, **113**, 3830.
- [19] P. K. Singh, P. K. Sharma, M. Kumar, R. Dutta, S. Sundaram, A. C. Pandey, *J. Mater. Chem. B*, 2014, **2**, 522.
- [20] A. K. Kole, C. S. Tiwary, P. Kumbhakar, *J. Appl. Phys.*, 2013, **113**, 114308.
- [21] D. Kim, M. Miyamoto, M. Nakayama, *J. Appl. Phys.*, 2006, **100**, 094313.
- [22] I. Broser, A. Hoffmann, R. Heitz, P. Thurian, *J. Lumin.*, 1991, **48**, 693.
- [23] S. S. Kumar, M. A. Khadar, K. G. M. Nair, *J. Lumin.*, 2011, **131**, 786.
- [24] S. Kar, S. Santra and H. Heinrich, *J. Phys. Chem. C*, 2008, **112**, 4036.
- [25] W. Wang, W. Zhu and H. Xu, *J. Phys. Chem. C*, 2008, **112**, 16754.
- [26] S. Zu, Z. Wang, B. Liu, X. Fan, G. Qian, *J. Alloys Compd.*, 2009, **476**, 689.
- [27] J. Y. Lee, D. S. Kim and J. Park, *Chem. Mater.* 2007, **19**, 4663.
- [28] D. S. Kim, Y. J. Cho, and J. Park, *J. Phys. Chem. C*, 2007, **111**, 10861.
- [29] A. Datta, S. K. Panda, S. Chaudhuri, *J. Solid State Chem.* 2008, **181**, 2332.
- [30] Y. Hsu and S. Lu, *Chem. Commun.*, 2004, **18**, 2102.
- [31] S. Biswas, S. Kar, S. Santra, Y. Jompol, M. Arif, S. I. Khondaker, *J. Phys. Chem. C*, 2009, **113**, 3617.
- [32] V. I. Nefedov, *J. Electron Spectrosc. Relat. Phenom.*, 1982, **25**, 29.
- [33] G. Deroubaix, P. Marcus, *Surf. Interface Anal.*, 1992, **18**, 39.
- [34] D. Chadwick, T. Hashemi, *Corros. Sci.* 1978, **18**, 39.

- [35] F. G. Fard, T. Hashemi, K. J. D. Mackenzie, C. A. Hogarth, *J. Mater. Sci.* 1983, **18**, 3679.
- [36] O. P. Tkachenko, E. S. Shpiro, M. Wark, G. S. Ekloff, N. I. Jaeger, *J. Chem. Soc. Faraday Trans.*, 1993, **89**, 3987.
- [37] J. S. Hammond, S. W. Gaarenstroom, N. Winograd, *Anal. Chem.*, 1975, **47**, 2194.
- [38] S. W. Gaarenstroom, N. Winograd, *J. Chem. Phys.*, 1977, **67**, 3500.
- [39] D. S. Kim, Y. J. Cho, J. Park, J. Yoon, Y. Jo, and M. Jung, *J. Phys. Chem. C*, 2007, **111**, 10861.
- [40] E. Agostinelli, C. Battistoni, D. Fiorani, G. Mattogno, M. Nogues, *J. Phys. Chem. Solids*, 1989, **50**, 269.
- [41] R. V. Siriwardane, J. A. Poston, *Appl. Surf. Sci.*, 1990, **45**, 131.
- [42] T. R. N. Kutty, *Mater. Res. Bull.*, 1991, **26**, 399.
- [43] M. Luo, Y. Liu, J. Hu, H. Liu and J. Li, *ACS Appl. Mater. Interfaces*, 2012, **4**, 1813.
- [44] O. P. Tkachenko, E. S. Shpiro, M. Wark, G. S. Ekloff, N. I. Jaeger, *J. Chem. Soc. Faraday Trans.*, 1993, **89**, 3987.
- [45] P. Narayan and E. Shlomo, *J. Phys. Chem. B*, 2004, **108**, 11964.
- [46] V. L. Mukta, G. Shubha, S. A. Acharya and S. K. Kulkarni, *Nanotechnology*, 2008, **19**, 415602.
- [47] J. Y. Lee, D. S. Kim, and J. Park, *Chem. Mater.*, 2007, **19**, 4663.
- [48] Z. X. Yang, P. Zhang, W. Zhong, Y. Deng, C. T. Au and Y. W. Du, *CrystEngComm*, 2012, **14**, 4298.
- [49] Y. Chen, X. Zhang, C. Jia, Y. Su and Q. Li, *J. Phys. Chem. C*, 2009, **113**, 2263.
- [50] V. Albe, C. Jouanin and D. Bertho, *Phys. Rev. B*, 1998, **57**, 8778.
- [51] A. A. Bol, A. Meijerink, *Phys. Rev. B*, 1998, **58**, 1599.

- [52] W. Peng, G. Cong, S. Qu, Z. Wang, *Opt. Mater.*, 2006, **29**, 313.
- [53] G. Murali, D. A. Reddy, G. Giribabu, R. P. Vijayalakshmi, R. Venugopal, *J. Alloys Compd.*, 2013, **581**, 849.
- [54] Y. M. Niquet, G. Allan, C. Delerue and M. Lannoo, *Appl. Phys. Lett.*, 2000, **77**, 1182.
- [55] M. S. Sander, R. Gronsky, Y. M. Lin and M. S. Dresselhaus, *J. Appl. Phys.*, 2001, **89**, 2733.
- [56] J. Cao, D. L. Han, B. J. Wang, L. Fan, H. Fu, M. B. Wei, B. Feng, X. Y. Liu, J. H. Yang, *J. Solid State Chem.*, 2013, **200**, 317.
- [57] K. Sooklal, B. S. Cullum, S. M. Angel and C. J. Murphy, *J. Phys. Chem.*, 1996, **100**, 4551.
- [58] E. S. F. Neto, N. O. Dantas, N. M. B. Neto, I. Guedes, F. Chen, *Nanotechnology*, 2011, **22**, 105709.

Figure captions

Figure 1. XRD patterns of (a) the $Zn_{1-x}Cd_xS$ NRs; (b) $Zn_{0.99-x}Cd_xCu_{0.01}S$ NRs; (c) $Zn_{0.99-x}Cd_xMn_{0.01}S$ NRs.

Figure 2. (a) (b) TEM images of the $Zn_{0.70}Cd_{0.30}S$ NRs; (c) HRTEM and FFT images of the $Zn_{0.70}Cd_{0.30}S$ NRs; (d) the enlarged HRTEM image of the yellow region in (c).

Figure 3. (a) (b) TEM images of the $Zn_{0.10}Cd_{0.90}S$ NRs; (c) (d) HRTEM and FFT images of the $Zn_{0.10}Cd_{0.90}S$ NRs; (e) the enlarged HRTEM and FFT images of the yellow region in (d); (f) the inverse fast Fourier transform (IFFT) image of the FFT image in (e).

Figure 4. (a) (b) TEM, HRTEM and FFT images of the $Zn_{0.69}Cd_{0.30}Cu_{0.01}S$ NRs; (c) (d) TEM images of the $Zn_{0.09}Cd_{0.90}Cu_{0.01}S$ NRs; (e) (f) HRTEM and FFT images of the $Zn_{0.09}Cd_{0.90}Cu_{0.01}S$ NRs; (g) the bright-field TEM image of the single $Zn_{0.09}Cd_{0.90}Cu_{0.01}S$ nanorod; (h-j) The EDS elemental mappings for Cd, Zn and S of the $Zn_{0.09}Cd_{0.90}Cu_{0.01}S$ nanorod in (g).

Figure 5. (a) (b) TEM images of the $Zn_{0.69}Cd_{0.30}Mn_{0.01}S$ and $Zn_{0.09}Cd_{0.90}Mn_{0.01}S$ NRs; (c) HRTEM and FFT images of the $Zn_{0.69}Cd_{0.30}Mn_{0.01}S$ NRs; (e) HRTEM image of the $Zn_{0.09}Cd_{0.90}Mn_{0.01}S$ NRs; (d) (f) the enlarged HRTEM images of the yellow region in (c) and (e).

Figure 6. (a) XPS survey spectra of the $Zn_{0.70}Cd_{0.30}S$ (red line), $Zn_{0.69}Cd_{0.30}Cu_{0.01}S$ (green line) and $Zn_{0.69}Cd_{0.30}Mn_{0.01}S$ (blue line) NRs; (b) (c) (d) High-resolution binding energy spectra of Zn 2p, Cd 3d and S 2p for the $Zn_{0.70}Cd_{0.30}S$ (red line), $Zn_{0.69}Cd_{0.30}Cu_{0.01}S$ (green line) and $Zn_{0.69}Cd_{0.30}Mn_{0.01}S$ (blue line) NRs; (e) (f) EDX spectra of the $Zn_{0.69}Cd_{0.30}Cu_{0.01}S$ and $Zn_{0.69}Cd_{0.30}Mn_{0.01}S$ NRs.

Figure 7. Room temperature PL spectra of the $Zn_{1-x}Cd_xS$ ($x=0.01, 0.05, 0.10, 0.30, 0.50, 0.70, 0.90$) NRs.

Figure 8. Room temperature PL spectra of (a) the $\text{Zn}_{0.99-x}\text{Cd}_x\text{Cu}_{0.01}\text{S}$ NRs ($x=0.05$, 0.10, 0.30, 0.50, 0.70, 0.90) NRs; (b) the $\text{Zn}_{0.99-x}\text{Cd}_x\text{Mn}_{0.01}\text{S}$ NRs ($x=0.05$, 0.10, 0.30, 0.50, 0.70, 0.90) NRs.

Figure 1

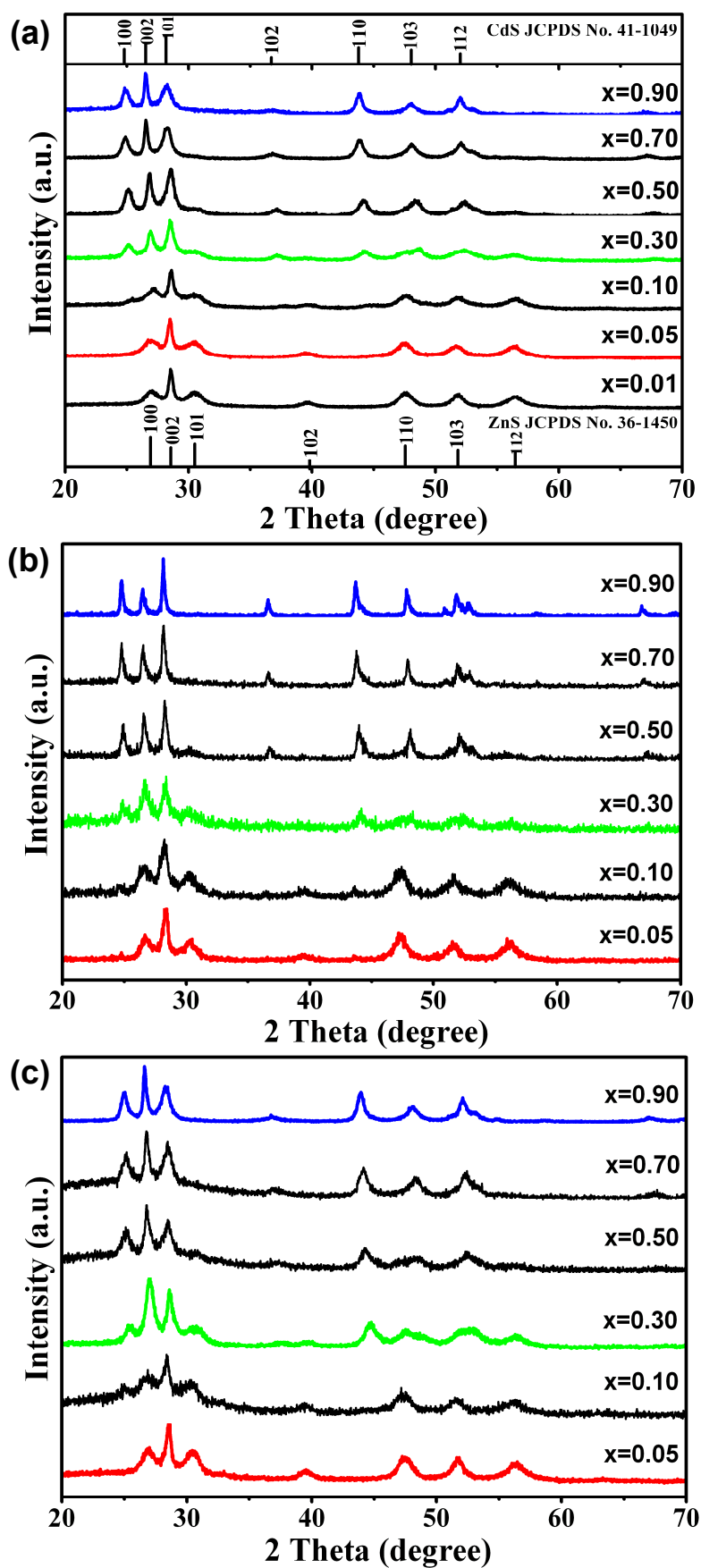


Figure 2

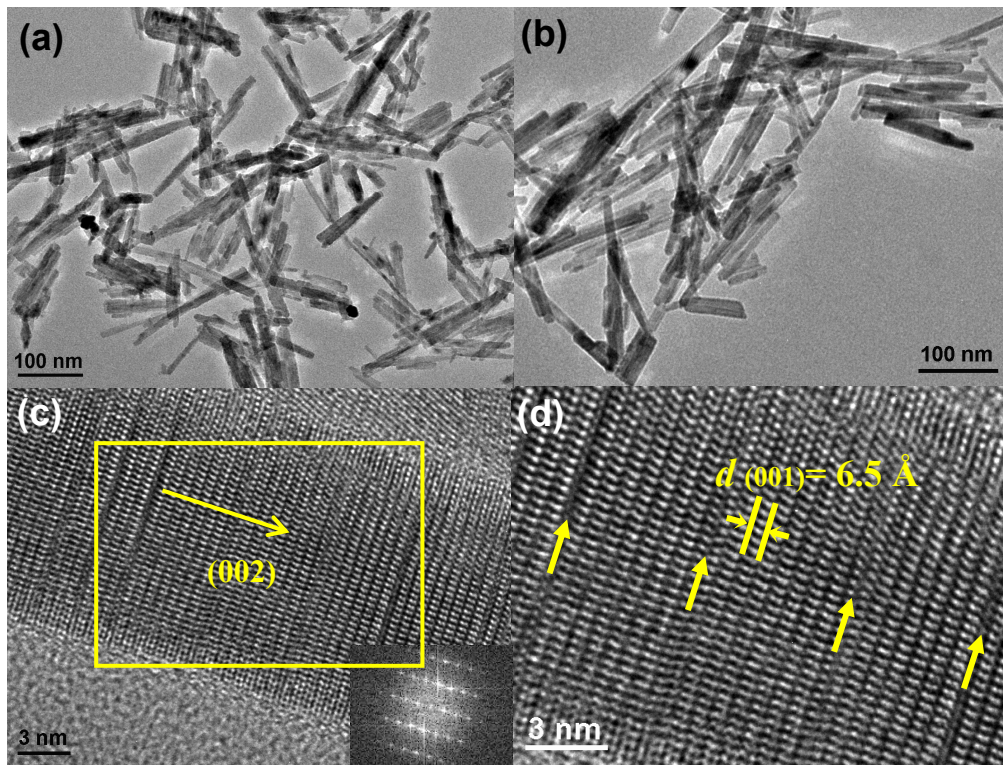


Figure 3

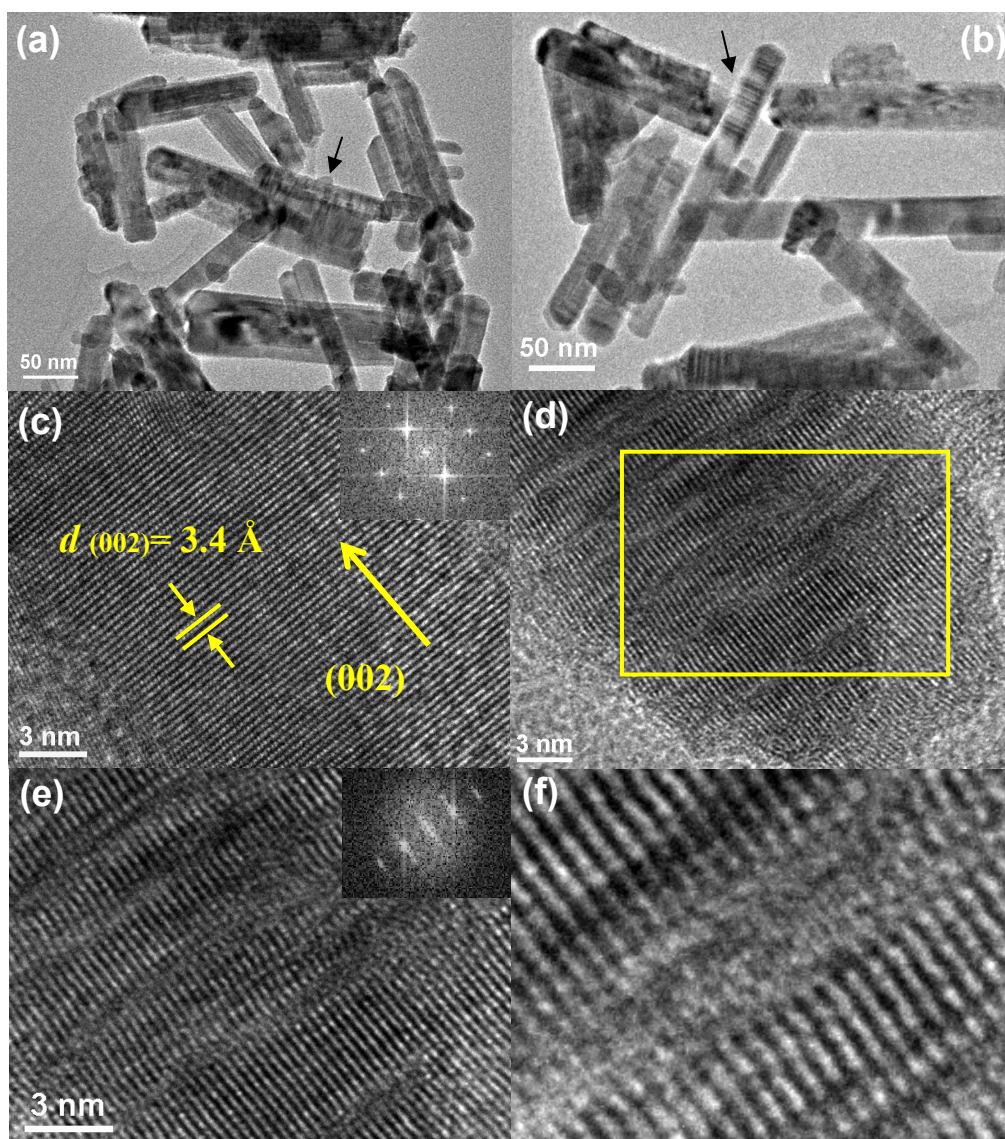


Figure 4

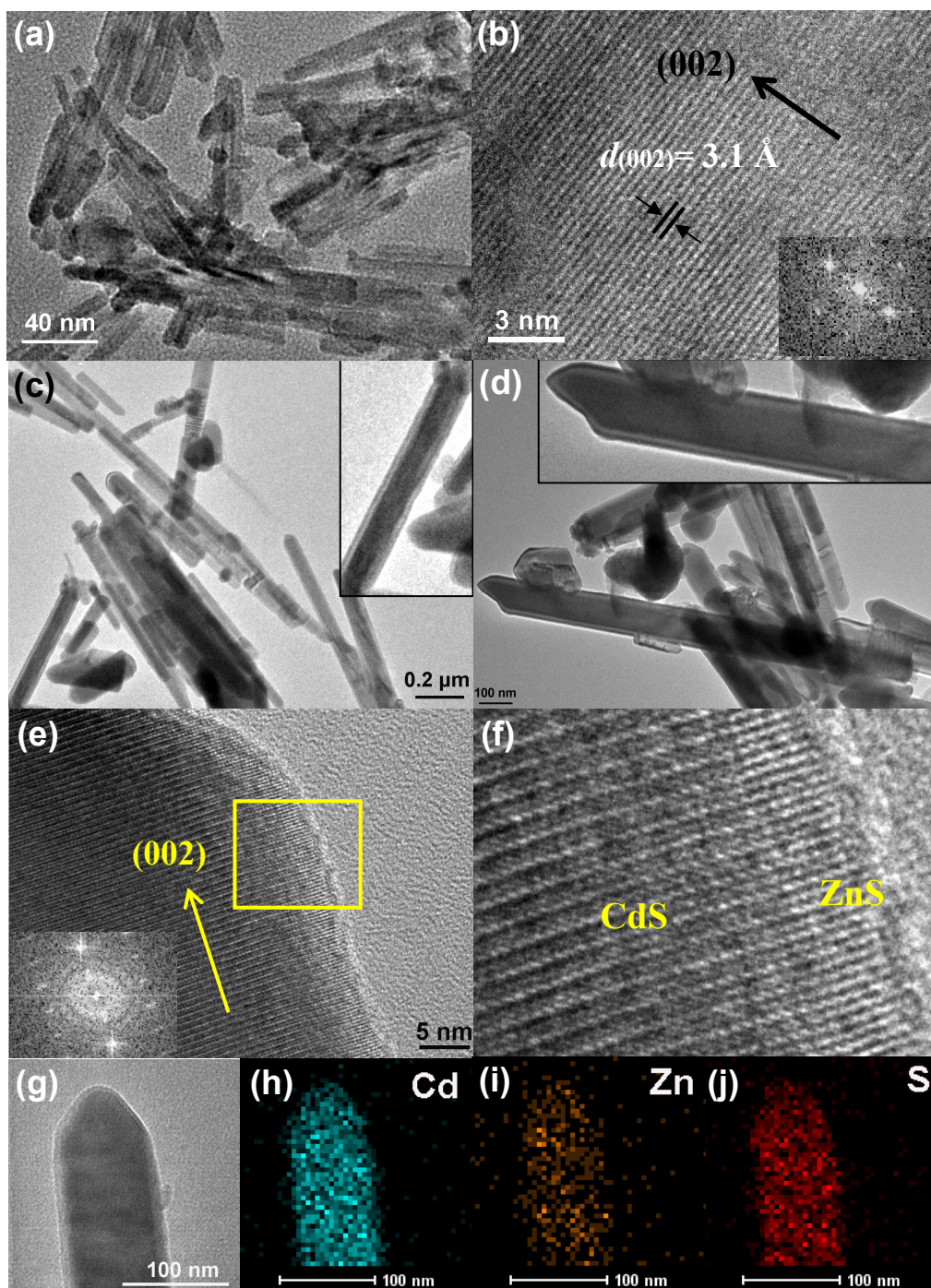


Figure 5

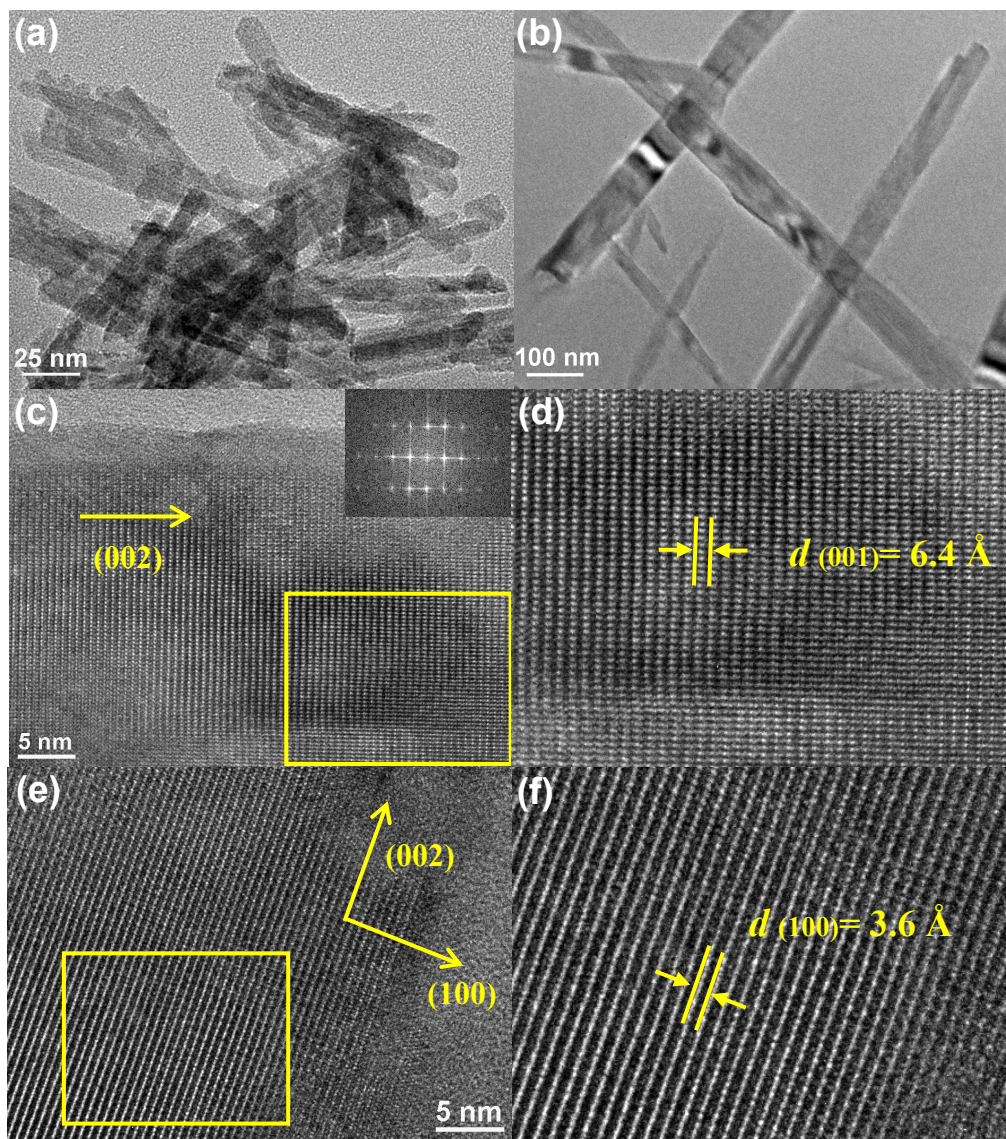


Figure 6

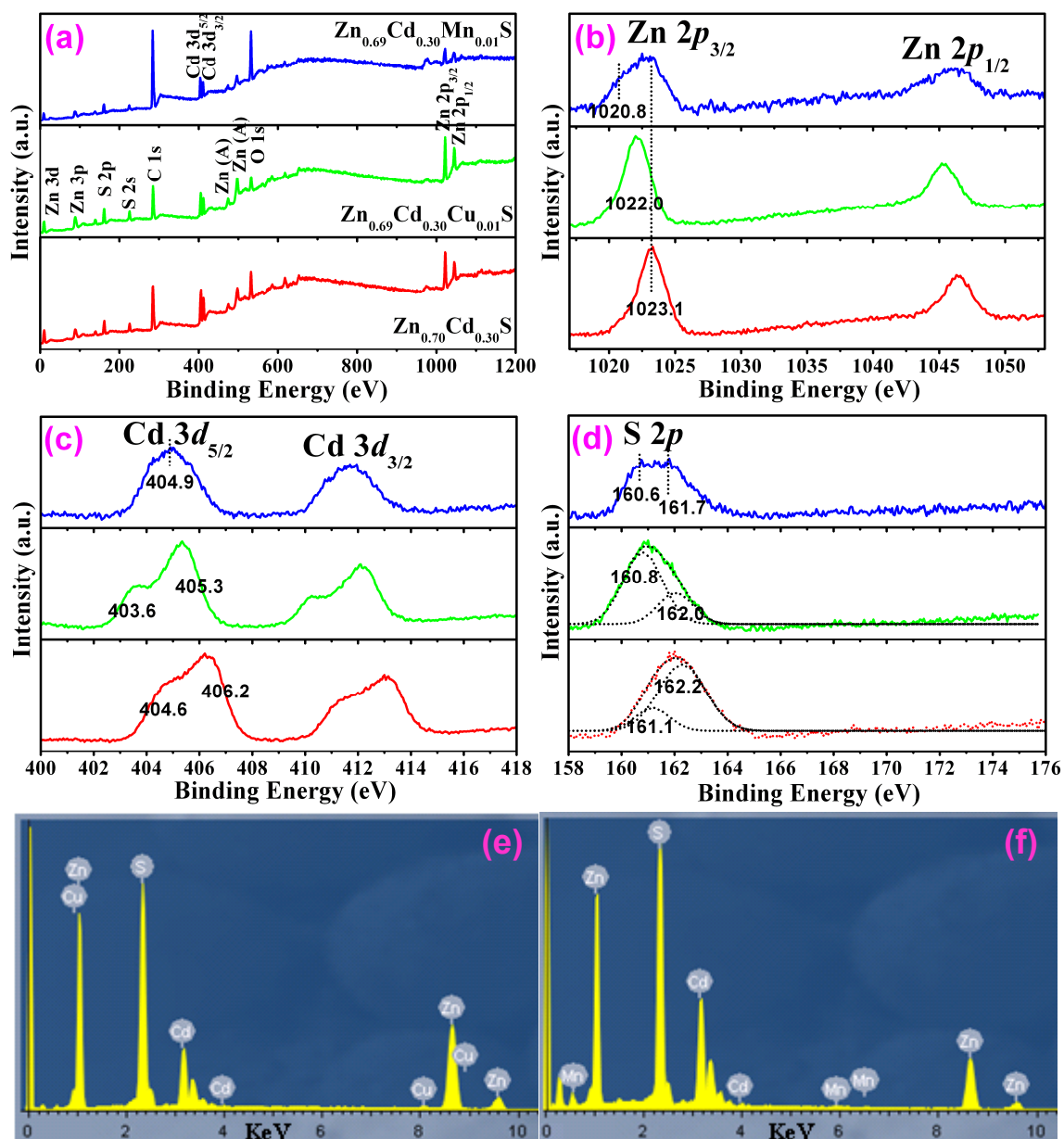


Figure 7

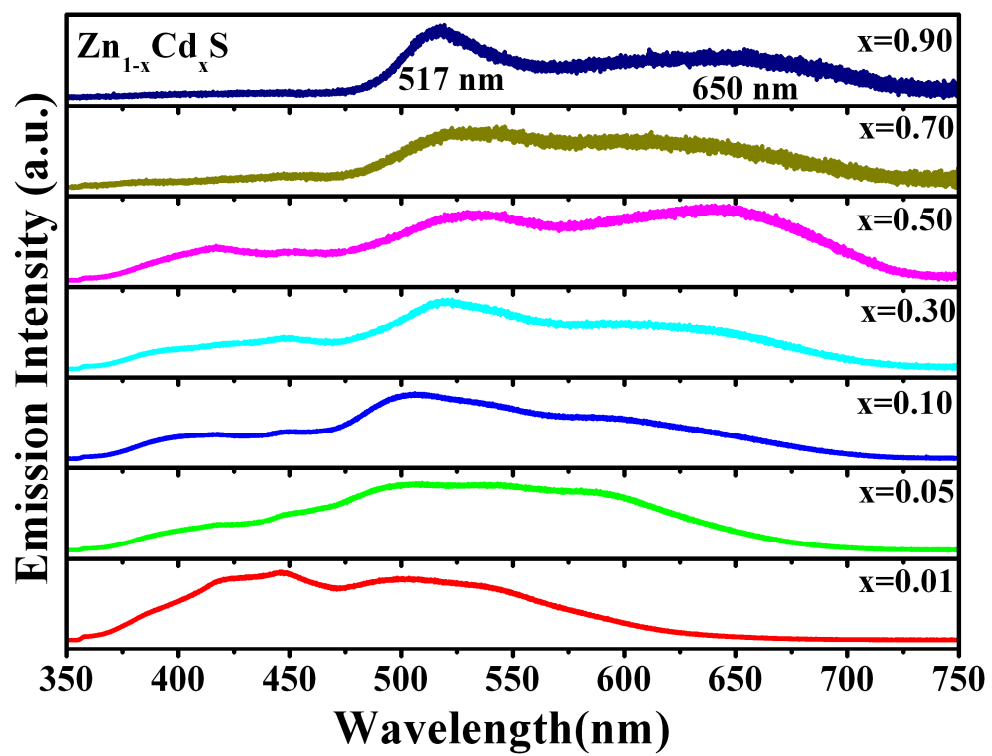
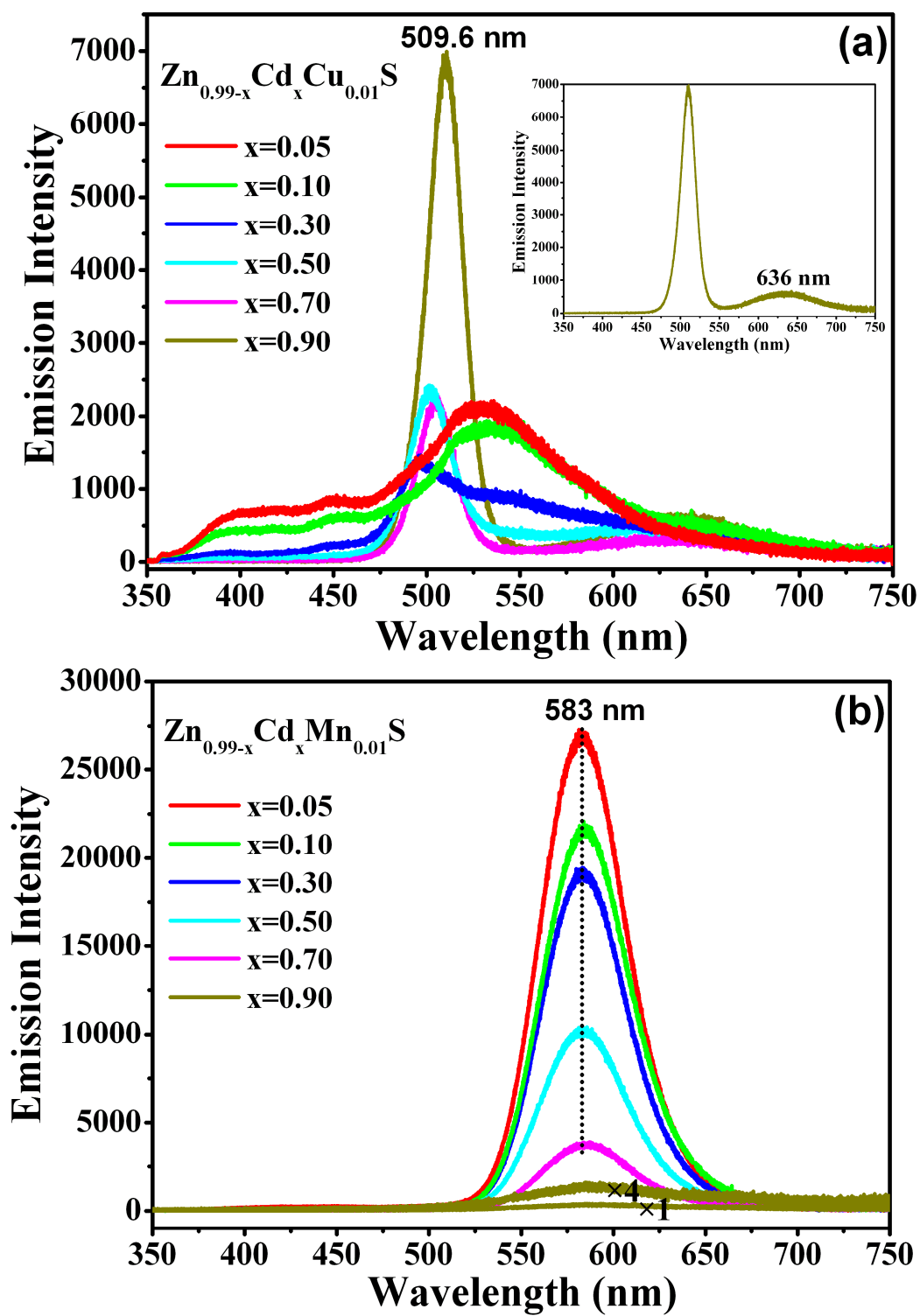
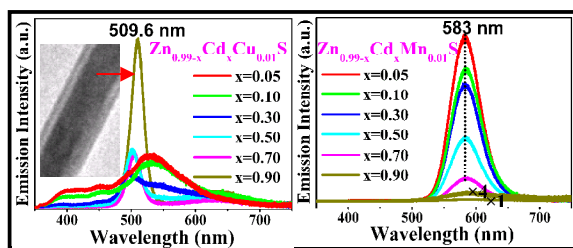


Figure 8





Doping Cu²⁺ and Mn²⁺ ions into Zn_{1-x}Cd_xS NRs make the samples exhibited a strong emission at 509.6 and 583 nm